Nullifying Tumor Efflux by Prolonged Endolysosome Vesicles: Development of Low Dose Anticancer-Carbon Nanotube Drug

Yeon Kyung Lee,[†,‡,#] Jungil Choi,[‡,#] Wenping Wang,[†,#] Soyoung Lee,[§] Tae-Hyun Nam,[†] Wan Sung Choi,[‡] Chang-Joon Kim,[⊥] Jong Kwon Lee,[∥] Sang-Hyun Kim,[§] Sang Soo Kang,[‡,*] and Dongwoo Khang[†,*]

[†]School of Nano & Advanced Materials Science, Bio-Nano-Information Tech. R/D Center and RIGET, Gyeongsang National University, Jinju 660-701, South Korea, [‡]Department of Anatomy, Institute of Health Science and School of Medicine, Gyeongsang National University, Jinju 660-751, South Korea, [§]Department of Pharmacology, Kyungpook National University Medical School, Daegu 700-422, South Korea, [⊥]Department of Chemical & Biological Engineering, Gyeongsang National University, Jinju 660-701, South Korea, and [∥]Toxicological Research Division, National Institute of Food and Drug Safety Evaluation, Ministry of Food and Drug Safety, Osong 363-700, South Korea. [#]These authors equally contributed to this work.

ABSTRACT As the majority of side effects of current chemotherapies stems from toxicity due to excessive dosing of anticancer drugs, minimizing the amount of drug while maximizing drug efficacy is essential to increase the life-quality of chemotherapy patients. This study demonstrated that the intracellular delivery of amide linked doxorubicin on carbon nanotube can nullify the efflux of cancer cells by achieving prolonged endolysosome delivery and can induce burst release of doxorubicin in an acidic hydrolase environment and, ultimately, can reduce the amount of anticancer drug by 10-fold compared to conventional effective drug dose. The clearance of accumulated carbon nanotubes in the liver was observed after 4 weeks, and analysis of liver toxicity markers showed no significant changes in GOT and GPT levels and release of pro-inflammatory cytokines across both short- and long-term periods.

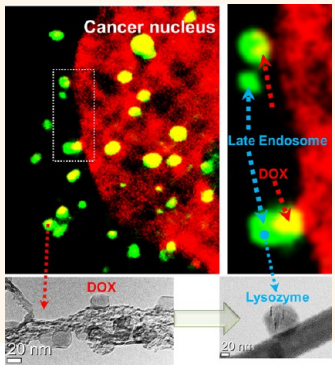

KEYWORDS: anticancer drug · amide covalent conjugation · doxorubicin · carbon nanotube · endolysosome delivery · liver toxicity

Although there have been tremendous efforts to overcome cancer with current chemotherapy, past strategies have elicited severe side effects in patients, such as cardio-toxicity, vomiting, hair loss, diarrhea and breathing troubles.[1−3] Greater dosing of anticancer drugs also increases toxicity to regenerated tissue and the immune system and, ultimately, diminishes the patient's quality of life.[4−6] Researchers now acknowledge that inhibiting the multidrug resistance (MDR) ability of resistive cancer cells is one of critical factors for reducing the dose of anticancer drugs.[7,8] However, co-treatment approaches that pair anticancer drugs with verapamil (VRP) and cyclosporine A (CsA) to inhibit MDR pumps interfered with their clinical applications due to their pharmacological toxicity, such as cardiovascular hypertension for VRP and immunosuppression for CsA.[9,10]

Another approach has been introduced to overcome drug resistance more effectively. For example, nanosized pharmaceutical agents, such as gold, silica, polymer, nanodiamond, and titanium nanostructures, have been suggested to reduce efflux from various cancer cells.[11−18] Specifically, recent development of nanomaterial-based drug delivery have focused on reducing drug efflux,[17,19−21] such as MDR gene silencing by attaching permeability glycoprotein-inhibiting small interfering RNA (P-gp-inhibiting siRNA) and targeting MDR-exhibiting cells. However, the instability of siRNA during blood circulation and the difficulty in targeting only MDR cells *in vivo* has hindered the clinical success as yet.[17,22,23]

Among the nanosized drug delivery agents, carbon nanotubes (CNTs) have been considered as a promising nanosized pharmaceutical agent for tumor suppression.[24−27] However, CNTs have not been extensively

* Address correspondence to dkhang@gnu.ac.kr, kangss@gnu.ac.kr.

Received for review May 2, 2013 and accepted September 12, 2013.

Published online September 12, 2013
10.1021/nn4041206

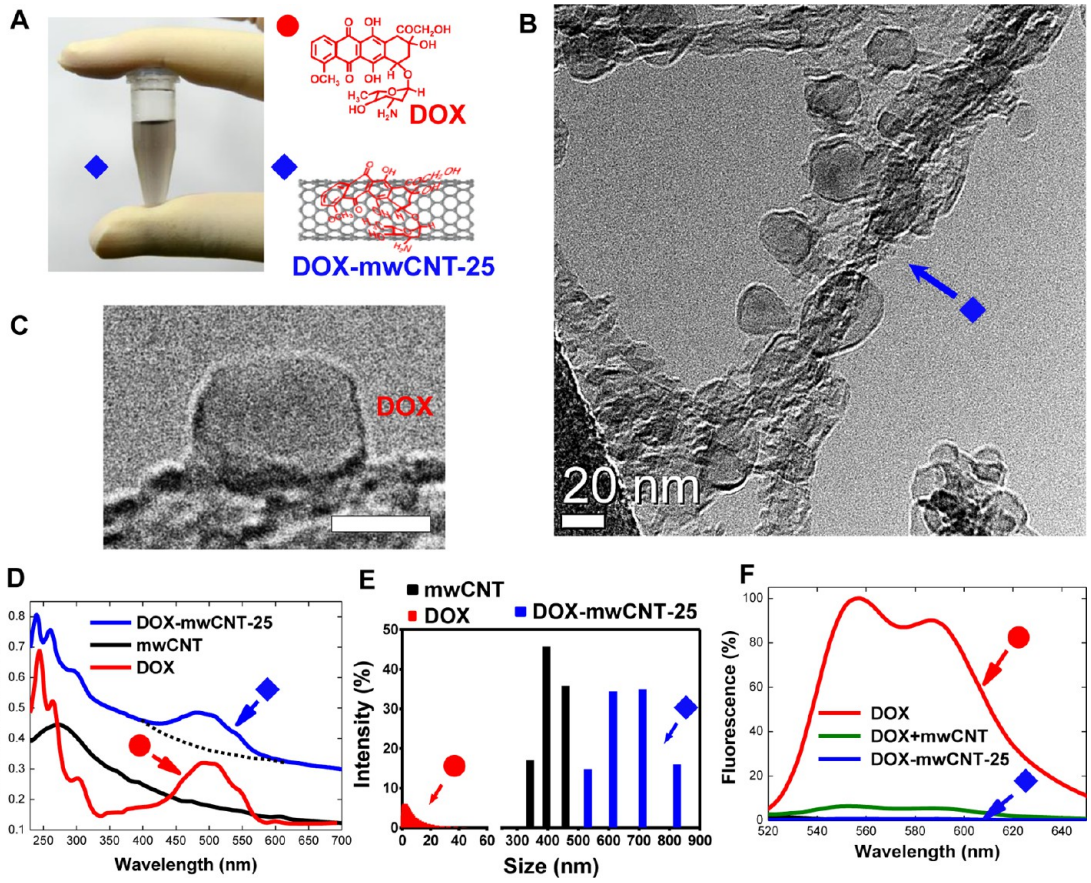

Figure 1. Physiochemical properties of covalently conjugated doxorubicin on mwCNTs. (A) Stored DOX-mwCNTs-25 in PBS. (B) Cryo-TEM images showing covalently attached DOX on mwCNTs. (C) Deformed shape of DOX represents evidence of strong conjugation with mwCNTs. Scale bar is 20 nm. (D) UV−vis showed the order of attached DOX on carboxylate mwCNTs (blue). DOX (red) and carboxylate mwCNT (black) were used as references for calculating amount of conjugated weight of DOX on mwCNTs. (E) Particle sizes of DOX, mwCNTs and DOX-mwCNTs in identical weight density in solution. covalently conjugated mwCNTs are generally larger than oxidized mwCNTs. (F) Complete quenching (*i.e.*, 99.2%) of DOX-mwCNT-25 was observed (blue), as compared to pure DOX by photoluminescence signals. This represents complete conformational change of DOX structures, as identified by the complete quenching of fluorescence signals by DOX.

considered as an effective drug influx mediator for reducing drug efflux despite efficient pharmaceutical *in vivo* results.[28−31] In general, noncovalent π stacking has been commonly used as a standard method to attaching drugs due to its greater drug loading efficiency (up to 200%).[25−27,32−34] However, in contrast to *in vivo* success, it is worth to note that the conjugation with π stacking was less effective in destroying cancer cells compared to conventional drugs, especially at low drug concentrations based on the previous *in vitro* studies.[27,35−38]

For designing a highly effective and low dose anticancer drug, two factors need to be considered. First, drug design should minimize drug release in extracellular environment before reaching the cancer cells. Second, intracellular drug delivery of nanoparticles should follow the endosome−lysosome without drug efflux. In this line, it is essential to design an anticancer drug whose conjugation type is stable in extracellular environments and intracellular drug delivery route should not interfered by efflux *via* MDR functions of cancer cells.[17,27] On the basis of these considerations, choosing an appropriate bioconjugation type is critical. The covalent conjugation is advantageous compared to noncovalent π stacking in terms of conjugation stability (drug release before reaching cells).[39] However, pure covalent linkages (without possessing noncovalent bonds) suffers from a low drug loading capacity of 10−15%[16,39,40] and has not shown clear scientific advantage to overcoming the low drug loading capacity as far.

This study demonstrated that optimized amide covalent conjugation of doxorubicin (DOX) on CNTs leads burst drug release at the vicinity of cancer nucleus through endolysosome intracellular pathways without cancer efflux and with increased drug stability and, ultimately, reduces 10-fold of conventional cancer drug. Furthermore, short and long-term liver toxicity markers by the distribution of anticancer carbon nanodrugs were investigated.

RESULTS

Maximizing Amide Covalent Linkages and Associated Conformational Changes of DOX on Multiwalled CNTs (mwCNTs). Doxorubicin was selected as the standard

anticancer drug in this study, as its common usage enables comparison to previously published studies (Figure 1A).[13,14,16,27] Enhancement of oxidization on nanotube surface is important not only to maximize covalent loading efficiency, but also to reduce toxicity to cells. The degree of carboxylic groups on mwCNTs was maximized to increase the number of available anchoring points for the covalent attachment of DOX through cross-linking with 1-ethyl-3-(dimethylaminopropyl)carbodiimide hydrochloride (EDC). Although previous studies suggested some promising aspect for the therapeutic treatment of cancer using covalent conjugation, ester covalent bond with 10-hydroxycamptothecin (HCPT)[39] and mixed states of $\pi-\pi$ bond (noncovalent) with hydrazone (covalent) bond on CNTs[39,41] suffered from low drug loading efficacy (not exceed 16%)[39] and partial covalent linkages on CNTs (major interaction is a noncovalent $\pi-\pi$ bonds),[41] respectively.

Through our suggested amide covalent linkage optimization process, weight ratio (weight of DOX/weight of mwCNTs) ranges are between 25 and 30% (defined as DOX-mwCNTs-25) in PBS solution (Figure 1A). Images obtained by cryo-transmission electron microscopy (Cryo-TEM, F20, Tecnai) shows covalently attached DOX on mwCNTs for the first time (Figure 1A,B). Most DOX molecules conjugated to carboxylate mwCNTs demonstrated a characteristic oval shape (Figure 1B). Particle sizes (averaged rotating length of nanotubes) of DOX, oxidized mwCNT, and DOX-mwCNT-25 showed length variation of 0−40, 350−450, and 500−830 nm, respectively (Figure 1E) and exhibited polydispersity ranging between 0.1 and 0.5, depending on the prepared sample densities in PBS (Figure 1E). The surface potential of DOX-mwCNT-25 shows reduced negative potential (−14 mV) compared to oxidized mwCNT (−33 mV). Strong covalent bonds between DOX and oxidized mwCNT were confirmed by luminescence quenching ratio using spectrophotometry and Raman spectroscopy (Figure 1F and Supporting Information Figure S3).[42−45] Due to amide functionalization, D/G ratio was increased on DOX-mwCNT-25 ($I_D/I_G = 2.3$), compared to mwCNT and physically mixed state of DOX and mwCNT ($I_D/I_G = 1.9$) (Supporting Information Figure S3). In addition, the 10% loading of covalently linked DOX (defined by DOX-mwCNT-10) on mwCNT reduced DOX fluorescence by 85.2%, which is comparable to previously reported data on the static quenching of DOX *via* π stacking (80−90% reduction of DOX fluorescence) (Supporting Information Figure S1C).[27,46] Notably, DOX-mwCNT-25 diminished DOX fluorescence by 99.2% (Figure 1F). This may be attributed to the photoinduced electron transfer (PET) by strong covalent linkage between DOX and mwCNT and indicated that the DOX structure had undergone conformational changes[42] through the coupled electron energy bands between DOX and oxidized mwCNTs (Supporting Information Figure S2C). The photoinduced effect of mwCNTs typically yields a higher quenching ratio as compared to single-walled CNTs (swCNTs).[47]

***In Vivo* Studies with 10-fold Reduction of DOX.** To examine the efficacy of developed DOX-mwCNT-25, MDA-MB-231 (malignant breast cancer cells that having efflux ability) xenografts were performed beneath the skin (see Materials and Methods for more details), and anticancer chemotherapy began when the tumor size exceeded 100 mm.[3] Bioaccumulation (or distribution) of DOX-mwCNT-25 in the liver and lungs showed more than 40% at both 30 min and 6 h after intravenous (IV) tail injection (Figure 2B,C). Heart, spleen, stomach, and intestine also showed greater accumulation of DOX-mwCNT-25, as compared to pure DOX after 30 min of IV injection (Figure 2B). This trend sustained for 6 h except in the heart (where most of the accumulation cleared after 6 h) (Figure 2C). The elevated blood flow in the heart may have accelerated the clearance rate of DOX-mwCNT from the heart by greater mechanical pumping. The kidney showed higher accumulation of pure DOX than of DOX-mwCNTs and this may be attributed to pure DOX undergoing clearance ahead of DOX-mwCNT by the urinary system. The accumulation percentage (2%) of DOX-mwCNT-25 in the tumor tissues was nearly identical to the allocation percentage presented from previous study (xenograft beneath the skin).[25]

The volume and mass of tumors treated with 0.5 mg/kg of DOX-mwCNT-25 were compatible with tumor mass of 5 mg/kg of pure DOX after three times IV injection (Figure 2D,E). In contrast, no notable tumor inhibition was observed on 0.5 mg/kg of pure DOX (Figure 2D−F). Tumor volume changes demonstrated a 6-fold increment of tumor volume for both 5 mg/kg of DOX and 0.5 mg/kg of DOX-mwCNT-25, as compared to a 30-fold increment of tumor volume in controls after 21 days (Figure 2F). No significant changes in body weight were observed during the experiments (Figure 2G). Hematoxylin and eosin (H&E) staining showed comparable tumor tissue necrosis in subjects treated with 5 mg/kg of pure DOX and 0.5 mg/kg of DOX-mwCNT. In contrast, no damage on tumor tissues was observed on subjects treated with PBS and mwCNT (Figure 2H). Although 0.5 mg/kg of pure DOX showed sporadic death of tumor tissue, the results did not correspond to significant tumor necrosis (Figure 2H). Furthermore, changes in Ki-67 (monoclonal antibody marker for cancer cell proliferation) expression confirmed comparable suppression of cancer proliferation for both 5 mg/kg of pure DOX and 0.5 mg/kg of DOX-mwCNT-25 (Supporting Information Figure S11).

***In Vitro* Studies at *in Vivo* Relevant Concentration.** Cancer cell viability test at *in vivo* relevant concentration (*i.e.*, low concentration) was examined. The effective drug

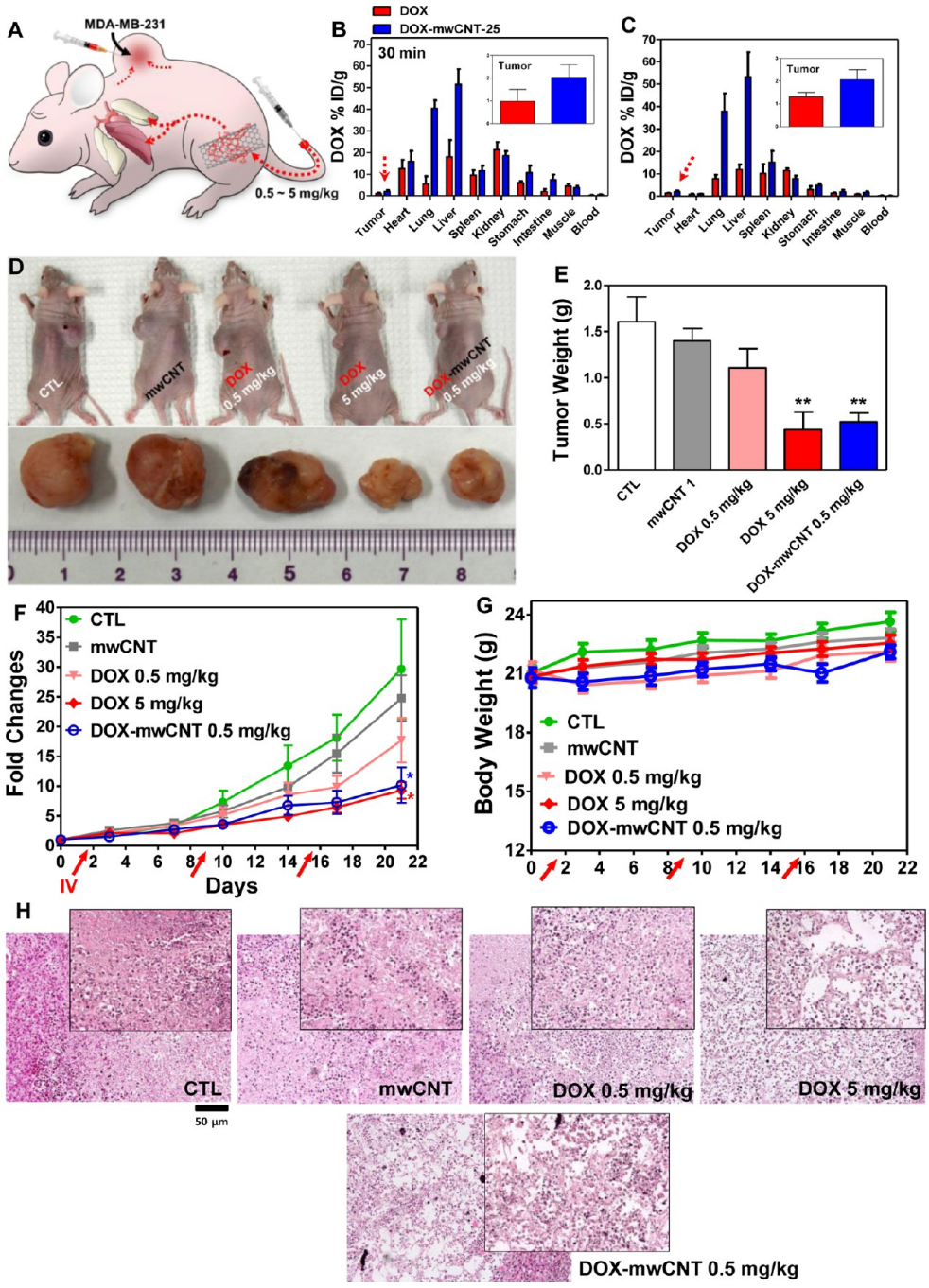

Figure 2. Equivalence of 10-fold less dose of DOX-mwCNT with conventional DOX. (A) Schematic representation of DOX-mwCNT injection to tumor-xenografted mouse model. (B and C) Biodistribution of DOX and DOX-mwCNTs in major organs at 30 min and 6 h after IV injection (2 mg/kg of drug concentration). Most organs showed greater accumulation of DOX-mwCNT, especially in the liver and lung. However, this was not observed in the kidney, where urinary system accelerated the clearance of DOX. DOX and DOX-mwCNTs accumulation in the heart were eliminated after 6 h. Only 2% of DOX-mwCNTs were detected in the tumor, whereas 1% of DOX was deposited in tumor tissues. (D) Tumor sizes of xenografted mice for various drug groups. Importantly, 5 mg/kg of DOX was equivalent to 0.5 mg/kg of DOX-mwCNTs. (E) Measured tumor weight for each group after 21 days. The 0.5 mg/kg of DOX-mwCNTs was effective at 10-fold reduction in concentration, as compared to conventional DOX drugs. (F and G) Tumor weight changes (represented as folds) show similar changes from 5 mg/kg of DOX and 0.5 mg/kg of DOX-mwCNTs. No notable body weight changes were observed. (H) H&E stains of each group showed severe damage on tumor tissue for both DOX 5 mg/kg and 0.5 mg/kg. No notable apoptosis was observed on PBS (CTL), mwCNT and DOX 0.5 mg/kg groups. Data represent mean ± SEM (n = 3 for biodistribution) and (n = 6−9 for tumor analysis).

concentration at tumor tissues depends on the allocated percentage from *in vivo* biodistribution. On the basis of the biodistribution after IV injection, only 1−2% of the administered dosage reaches the cancer tissue (Figure 2B,C). Numerically, the anticipated amount of anticancer drugs in tumor tissue, after 0.5 mg/kg of IV injection, would be less than 200 ng/mL (or less than 344 nM, see Materials and Methods).

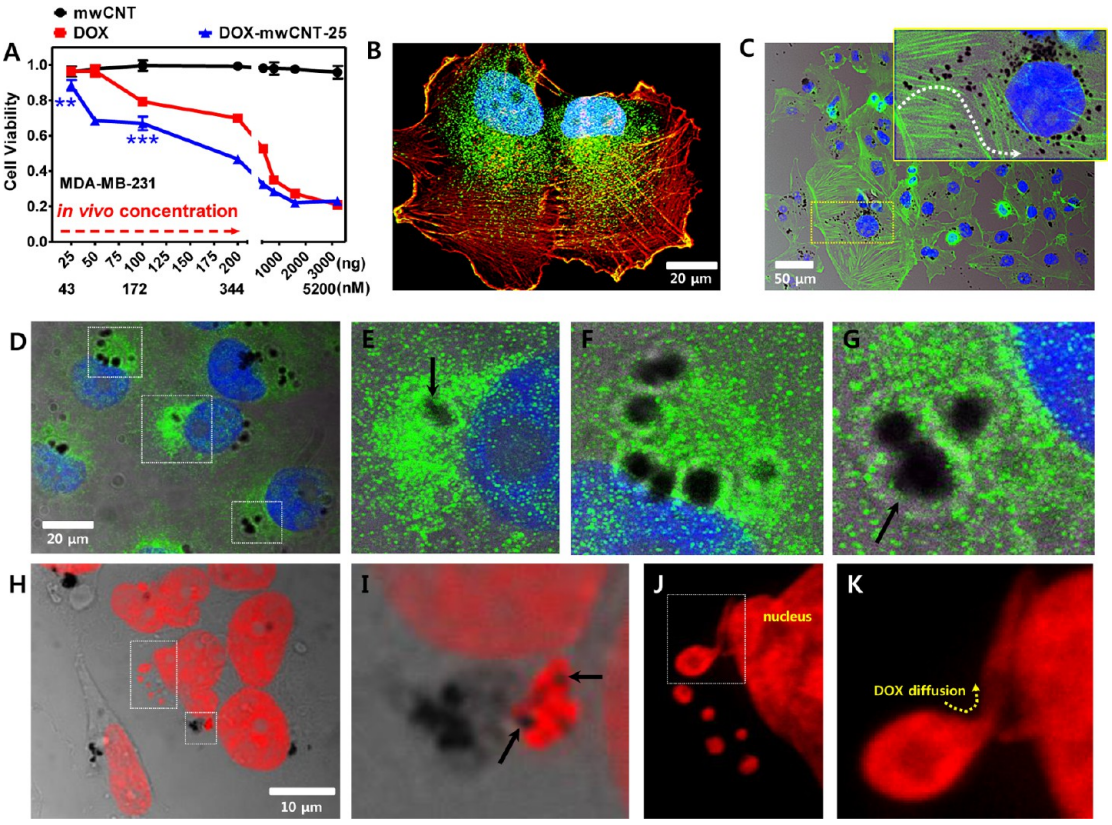

Figure 3. ***In vitro*** **cell viability at** ***in vivo*** **relevant concentrations. (A) MDA-MB-231 cell viability by increasing** ***in vivo*** **DOX concentration. MDA-MB-231 showed significant change in cell viability was observed at very low concentration. (B) Increasing lysozyme densities as approaching to nucleus in MDA-MB-231. (C) Immunostaining of MDA-MB-231 showed higher networks between cells after treated with mwCNTs (at concentration of 650 ng/mL). Magnified image (inset) represented the endocytosis−endosome−lysosome pathway of mwCNTs to nucleus in MDA-MB-231 cells. This image suggested evidence of identical DOX-mwCNT delivery to cancer cells after uptake. (D) Lysozyme densities after intake of mwCNTs in MDA-MB-231 cells. (E−G) Magnified images showed vesicle formations enclosing mwCNTs surrounding nucleus with greater densities of lysozymes. (H) DOX-mwCNTs-25 treated cells showed identical vesicle formations enclosing mwCNTs. (I) Demonstration of endolysosome enclosing DOX-mwCNTs. (J and K) Magnified image captured from h showing direction of DOX diffusion from endosome-like vesicles to cell nuclei.**

At *in vivo* drug concentration, cell viability of MDA-MB-231 cells was greatly arrested by DOX-mwCNT-25 (Figure 3A). A concentration of 25 ng/mL (43 nM) was sufficient to obtain a statistical difference in cell viability (Figure 3A). The viability of MDA-MB-231 cell at 50 ng of DOX-mwCNT-25 was comparable to that at 200 ng of pure DOX and this suggested that DOX-mwCNT-25 was 4 times more effective than pure DOX at low drug concentrations (Figure 3A). MDA-MB-231 morphology exhibited higher cytoskeletal networking and greater cell aggregation on at control samples. The increased lysozyme density as approaching to nucleus in MDA-MB-231 suggested a favorable environment for cleaving of amide bonds between DOX and mwCNTs (Figure 3B,D−G). Samples with pure mwCNTs also showed identical cytoskeletons and networking compared with control samples (Figure 3C).

Among the several mechanisms of nanoparticle-assisted drug delivery, the endocytosis pathway was considered as a major pathway due to size of nanomaterials.[48] The inset image in Figure 3C illustrates the endocytosis assisted pathway of mwCNTs into the nucleus in MDA-MB-231 cells. This represented the general route of DOX-conjugated mwCNTs after cellular uptake. Magnified images showed vesicle formations enclosing mwCNTs surrounding nucleus with greater densities of lysozymes (Figure 3D−G). This suggested evidence of vesicles (either late endosomes or lysosomes) enclosed with mwCNTs were transported to regions abundant with hydrolytic enzymes in the vicinity of nucleus (Figure 3D−G). DOX-mwCNTs-25 treated cells showed identical vesicle formation enclosing mwCNTs, providing evidence toward endosome and lysosome enclosure of DOX-mwCNTs (Figure 3H). Magnified images show DOX diffusion from endosome-like vesicles to the cell nucleus. Detailed analysis on these images will comprehensively be discussed in next section. In addition, competition of cell proliferation arrest for PEG coated liposomal DOX (DOXIL: Doxoves) and developed DOX-mwCNT-25 was analyzed. Cell viability shows greater cancer proliferation inhibition on DOX-mwCNT than that on DOXIL and DOX (Supporting Information Figure S5).

To examine the efficacy of DOX-mwCNT drugs on other cancer cell types, MCF-7 (breast cancer cell) were treated with DOX-mwCNT-10 and DOX-mwCNT-25 (*i.e.*, 10% and 25% loading, respectively) at low concentrations (*i.e.*, less than 100 ng/mL or 0.2 μM). Results indicated that both loading concentrations showed enhanced efficacy in inhibiting proliferation of MCF-7 over pure DOX (Supporting Information Figure S4A). To evaluate the response of noncancerous healthy cells, NIH3T3 fibroblasts were also examined (Supporting Information Figure S4C). Fibroblast response resembled cell viability of MCF-7, but cellular response showed a moderate difference between DOX-mwCNT-25 and pure DOX at very low concentration (Supporting Information Figure S4B, C). The different cell response of DOX-mwCNT-25 for MCF-7 and NIH3T3 at very low drug concentration is not elucidated and needs to be examined by further study.

Mechanism I: Late Endosome–Lysosome Delivery and Burst Drug Release in Acidic Lysozyme Condition. Examining sequential endocytic initiated pathways is an essential step to understanding drug delivery at the intracellular level. The advantage of endosome delivery of DOX-mwCNTs mechanism is that this type of vesicles usually does not experience drug efflux from cytosol into the extracellular space. Analysis of late endosome marker provided direct observation of intaked DOX-mwCNTs before its transport into lysosomes or Golgi because the late endosome stage is located between early endosome (approaching drug) and lysosome (degrading drug). Although previous studies discussed the possible endosome and lysosome delivery of nanodrugs, no clear evidence determined whether the endosome or lysosome is the drug releasing point from nanoparticles. Figure 4A–G provided evidence of drug release during the endolysosome stage because observed DOX was abundant in late endosome while DOX was depleted in lysosomes. Magnified images of late endosome showed diffusion of DOX from late endosome to nucleus (Figure 4C, Supporting Information Figure S14A–C). To the best of our knowledge, this is the first demonstration of DOX release from nanoparticles enclosed in late endosome. DOX and lysosome images showed simultaneous presence of approaching endosomes (red: DOX in early or late endosomes) and outgoing lysosomes (green) with depleted DOX in vesicles (Figure 4D–F). Magnified image shows diffusion of DOX from lysosome vesicles with a DOX-enclosed endosome in the vicinity (Figure 4G). As greater lysozymes were found at the vicinity of nuclei of MDA-MB-231 cells, abundant acid hydrolases surrounding nucleus, enclosed in late endosomes and lysosomes, possess sufficient protease enzymes to cleave amide conjugations between DOX and mwCNT (Figure 3B). To understand the observed phenomenon, *in vitro* drug release experiments were performed to understand the burst release of DOX from covalently conjugated mwCNT during endolysosome pathway. First, outer cell environments (PBS) showed no distinct release of DOX as time advance (*i.e.*, up to 240 h) (Figure 4J). DOX release in 10% FBS showed incremental release of DOX over time, suggesting that DOX-mwCNT bonds were slowly degraded across many hours under hematological environments (Figure 4J). Furthermore, linkages of designed drugs were highly stable in both neutral and acidic condition (Figure 4J). Thus, drug release analysis presents a designed DOX-mwCNT anticancer drug that is highly stable under extracellular conditions. Furthermore, drug release under intracellular conditions was also examined. Remarkably, notable release in high lysozyme density in neutral condition (pH = 7) was observed and significant burst release was achieved by simultaneous exposure to an acidic environment and greater lysozyme density (Figure 4J). The observed release supported the observation that optimized conditions for cleaving covalently linked DOX to mwCNTs requires acidic hydrolase. Considering late endosomes and lysosomes are composed of 40 types of acidic hydrolases, including lysozymes, the obtained data provided evidence of a highly selective release of DOX during late endosome and lysosome stages. Lastly, cryo-TEM images showed evidence of DOX cleave from mwCNT and lysozyme attachment onto mwCNTs (Figure 4H,I). Various shapes corresponding to lysozyme crystallizations were identified by diffraction patterns in Cryo-TEM images (Figure 4I). Importantly, it was concluded that developed DOX-mwCNT-25 induced many endosome vesicles compared to DOX and DOXIL and, thus, provided a more favorable condition than conventional drugs (DOX and DOXIL) for nullifying efflux working system of tested cancer cells (see Supporting Infromation Figure S11). In conclusion, it was observed that the developed DOX-mwCNTs were transported into the nucleus through late endosome and lysosome formation. In addition, *in vitro* drug release analysis and Cryo-TEM images confirmed the abrupt release of DOX under acidic-lysozyme condition.

Mechanism II: Prolonged Delivery of DOX-mwCNT through Endosome Vesicle and Efflux Nullification. Individual analysis on intake and efflux by increasing drug dose and time advance is a critical step for evaluating the efficacy of developed drugs. At *in vivo* targeting concentrations, no significant difference in intake was observed between the amount of pure DOX and DOX-mwCNT-25 during the initial 2 h after drug incubation (Figure 5C, Supporting Information Figure S6) in MDA-MB-231 cells. This trend sustained even with increasing drug dosing. However, significant changes were observed after 12 h, when intake and efflux simultaneously occurred (Figure 5D, Supporting Information Figure S7). This effect became more distinct by increasing drug concentration (*i.e.*, from 10 to 200 ng/mL). Since no significant differences were observed with intake,

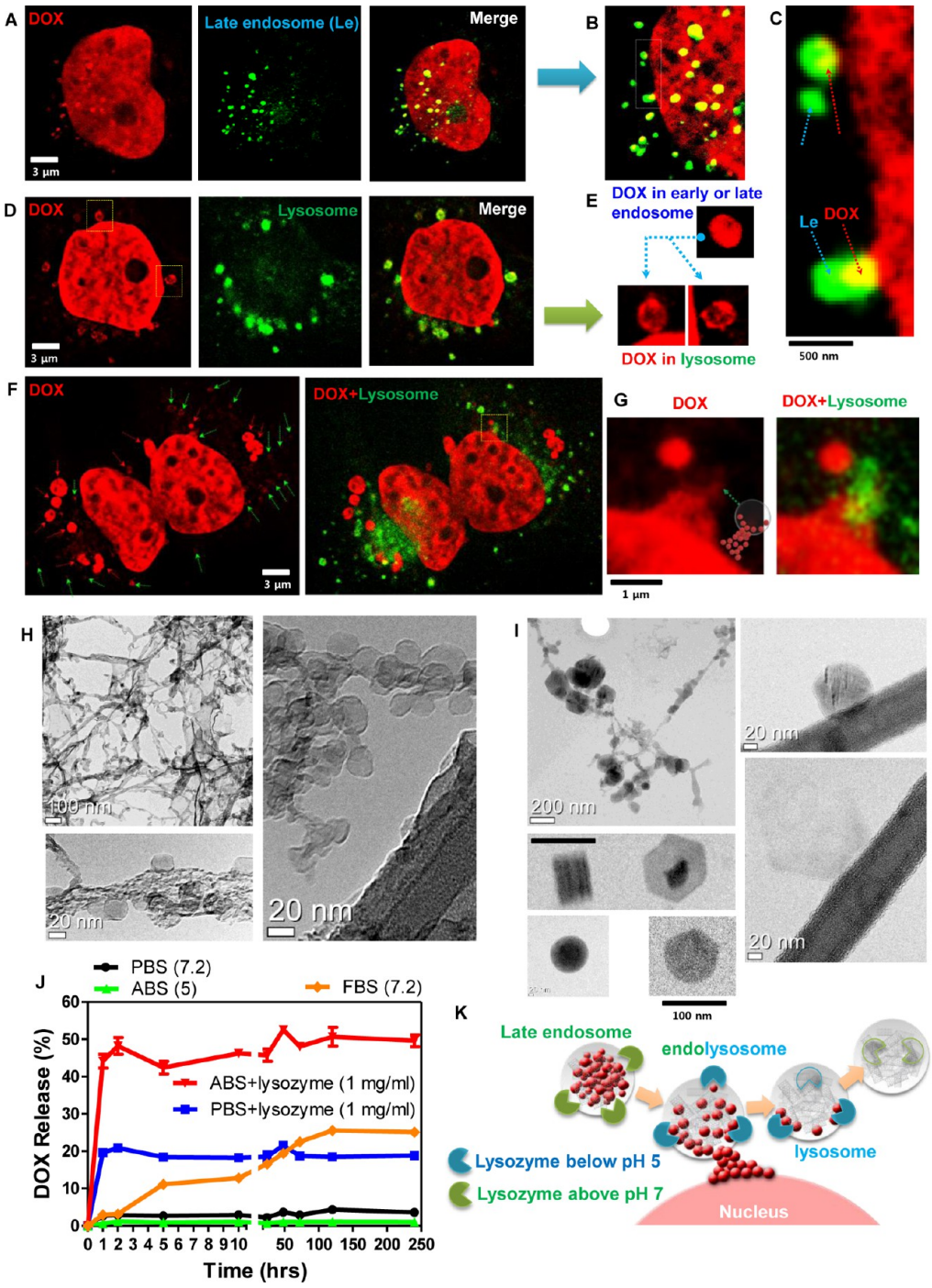

Figure 4. Late endosome–lysosome delivery with burst DOX release in acidic lysozyme condition. (A) Co-staining with DOX (red) and late endosome (Le: green) exactly matches same spots surrounding cancer nucleus. (B) Magnified images show approaching late endosomes to cancer nucleus and late endosome vesicles emerged from the nucleus. (C) High resolution image identified DOX diffusion (yellow) from late endosome (green) to nucleus (red). (D–F) Co-staining with DOX (red) and lysosome (green) showed direct overlap surrounding cancer nucleus. Whereas DOX (red) was abundant in late endosome, lysosome stage shows less DOX intensity, indicating DOX depletion in vesicles. This provided evidence of DOX release during endolysosome stage (*i.e.*, burst release between approaching late endosomes (greater DOX) and outgoing lysosomes (less DOX)). (G) Magnified image showed diffusion of DOX from lysosome vesicles while approaching another endosome enclosing DOX. Leftover DOX around late endosome vesicles shows final stage of DOX depletion through lysosome stage. (H) Cryo-TEM images show covalently linked DOX on mwCNTs, and this corresponds to vesicles until late endosome stage. (I) Cry-TEM images show removed DOX by cleaving amide bond through lysozymes and attachment of lysozymes on mwCNT (instead of DOX). This corresponds to vesicles after lysosome stage. (J) Drug release at different pH (pH 5 and 7.2), FBS, and different pH of lysozyme (1 mg/mL of lysozyme density). This environment resembles typical late endosome and lysosome conditions. Stable conjugation by change of pH and slow release by FBS were observed. However, sudden release (by cleavage of covalent bonds) of DOX was observed by adding neutral lysozyme. Enhanced release was observed under acidic lysozyme condition. (K) Schematic representation of late endosome–lysosome delivery with burst drug release at endolysosome stage.

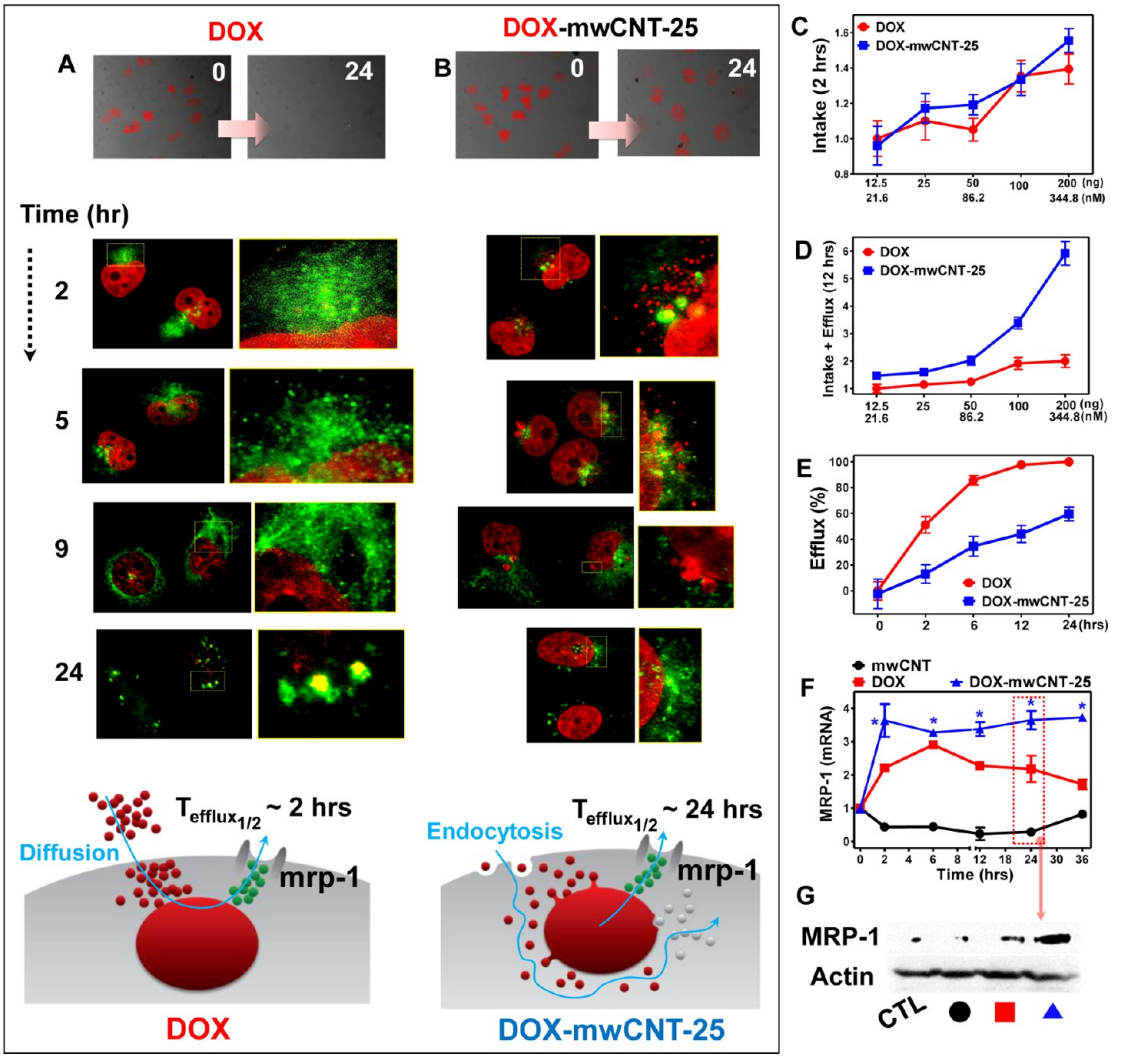

Figure 5. Prolonged delivery of DOX-mwCNT through endosome vesicle and efflux nullification. (A) Pure DOX had undergone efflux during 6−24 h by MDA-MB-231 cells and negligible amounts of late endosomes were observed after depletion of DOX in the nucleus. (B) On the contrary, 60% of DOX-mwCNT-25 and late endosome signals remained even after 24 h. (C) Intake (for 2 h) showed no noticeable difference between DOX and DOX-mwCNT-25. (D) Significant difference was observed after 12 h of incubation between the two groups with increasing drug concentration. This demonstrated a difference between intake and efflux of DOX-mwCNT-25 and pure DOX. (E) Efflux analysis by incubation with the drug for 2 h and subsequent exchange with new media showed that cancer cells completely ejected intaked-DOX by pumping out (*i.e.*, efflux) after 12 h, whereas DOX-mwCNT-25 showed only 40% of drug pumping out. (F and G) Strong activation of *Mrp-1* mRNA expression on DOX-mwCNT-25 after 2 h (*i.e.*, after intake) and sustained until 36 h, whereas *Mrp-1* function of DOX-intaked cancer cells diminished after 6 h. Western blotting of MRP-1 at 24 h exactly matches the mRNA expression results. The applied drug concentration was 500 ng/mL for (A) and (B) and was 100 ng/mL for (C−G).

results corresponded to the difference in efflux between DOX and DOX-mwCNT-25. Efflux analysis was performed by allowing cells to incubate at an *in vivo* relevant concentration of 100 ng/mL for 2 h and samples were subsequently exchanged with fresh media (*i.e.*, without drug dosing). It was observed that 60% of DOX-mwCNT-25 remained in MDA-MB-231 cells after 24 h, whereas pure DOX had completely undergone efflux during 6−12 h by MDA-MB-231 cells (Figure 5E, Supporting Information Figure S7). Similar trends were observed on the efflux analysis with DOXIL (see Supporting Information Figure S10 for more detail). On the basis of the clearance studies, it was concluded that developed DOX-mwCNT-25 possessed greater efflux nullification ability than DOX and DOXIL. Interestingly, only 2 h intake (or exposure) of DOX-mwCNT-25 (100 ng/mL of concentration) resulted in a notable difference in cell viability after 48 h (Supporting Information Figure S13A). High magnification image analysis showed the degradation of intake DOX signals (efflux-on system), which was examined for 24 h by the co-staining of DOX and late endosome marker. Importantly, negligible amount of late endosomes was observed after complete depletion of DOX from the nucleus as observed by fluorescence microscopy at high resolution (Figure 5A). As such, it was concluded that the late endosome acted as an outgoing transporter of effluxed DOX from the nucleus. In contrast,

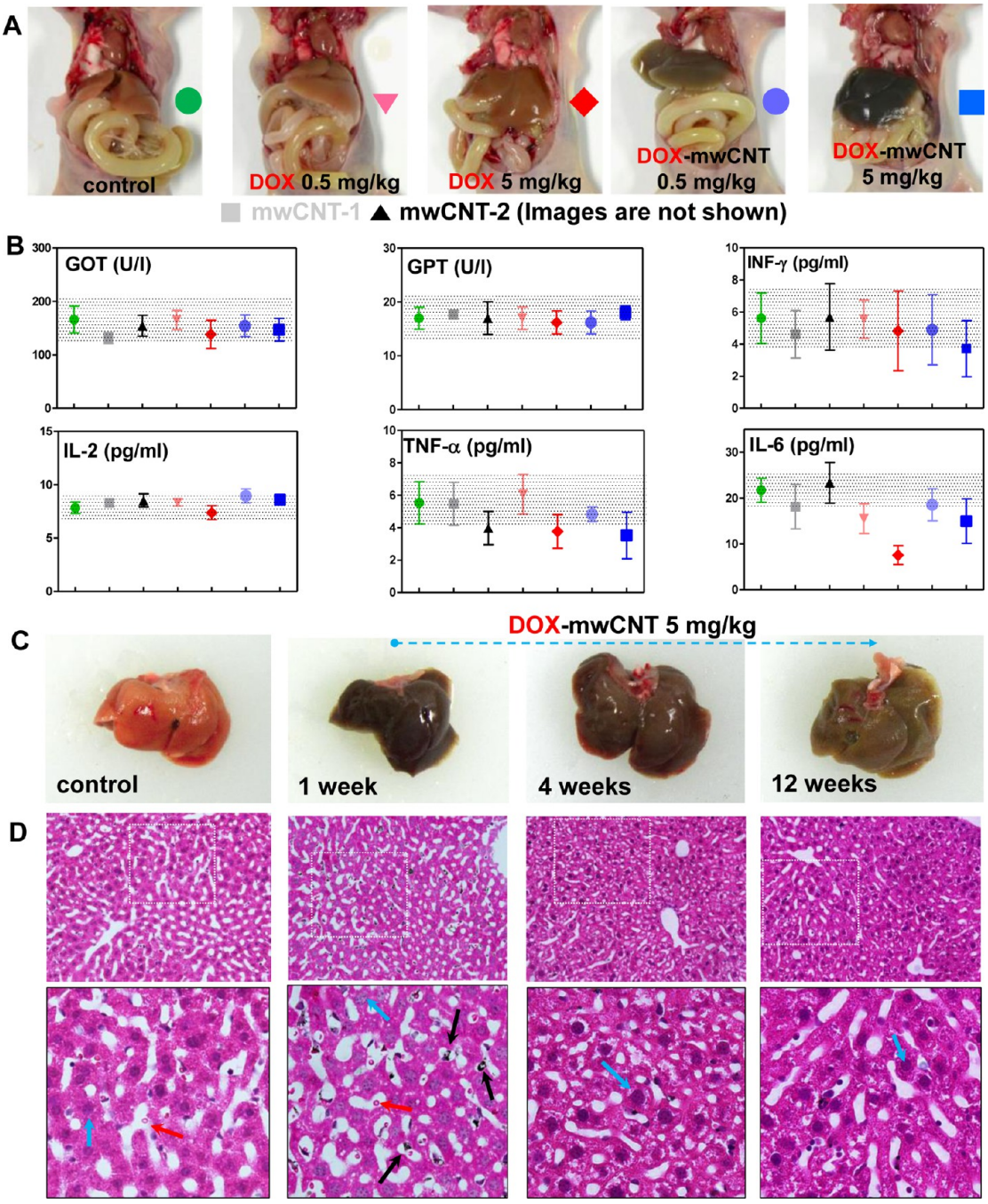

Figure 6. Liver toxicity, inflammation and clearance. (A) Images of liver color changes from increased mwCNT accumulation. (B) GOT, GPT, TNF-α, IFN-γ, IL-6 and IL-2 levels of each groups compared to normal ranges. No notable changes in toxicity and in cytokine levels were observed. (C) Liver clearance for 5 mg/kg of DOX-mwCNT after 1, 4, and 12 weeks. (D) H&E stains shows accumulation of aggregated mwCNTs (black arrows) and red blood cells (red arrow) in microvasculature between hepatocytes (cyan arrows). After 4 weeks, CNT aggregates disappeared. Data represent mean ± SEM (n = 5).

late endosome signals were not diminished in the nucleus of DOX-mwCNT-25 treated cell for 24 h (Figure 5B).

Furthermore, it was identified that a greater amount of early endosome vesicles enclosing DOX-mwCNT-25 (as inferred from the higher DOX intensity observed within the vesicles) infusing on the nucleus was identified even after 24 h. This is the first finding that endosome vesicles enclosing DOX-mwCNT-25 continuously approach and release DOX into the nucleus through endosome or late endosome vesicles even after 24 h by just 2 h of DOX-mwCNT exposures (Figure 5A,B). Although DOXIL showed some endosomes enclosed with DOXIL approaching to nucleus, the number of endosome vesicles inside cytosol were less than DOX-mwCNT-25 (see Supporting Information Figure S11). Analysis of *Mrp-1* (multidrug resistance-associated protein-1) mRNA and MRP-1 Western expression

showed different efflux working mechanisms between DOX and DOX-mwCNT-25 treated cells. Time advance analysis of mRNA expression of *Mrp-1* showed maximal expression at 6 h after cellular intake of DOX, whereas DOX-mwCNT-25 still showed up-regulated MRP-1 expression that sustained for at least 36 h (Figure 5F). To confirm this at the protein level, MRP-1 protein synthesis was confirmed at 24 h and Western blotting showed a significant difference in the protein expression of MRP-1 between DOX and DOX-mwCNT-25 (Figure 5G, Supporting Information Figure S12B). Specifically, MRP-1 protein synthesis remained up-regulated for DOX-mwCNT samples, as compared to the weak Western band of MRP-1 for pure DOX samples at 24 h. Even though *Mdr-1* and *Mrp-1* genes have been reported to mediate efflux for MDA-MB-231,[49] only *Mrp-1* expression was barely detected in this experiment because of short time of drug exposure to cells (2 h).

To the best of our knowledge, our obtained results are the first demonstration of efflux nullification by the prolonged endosome delivery of DOX-mwCNTs without the gene silencing of multiple drug resistance-1 (*Mdr-1* or *P-gp*) to overcome efflux in cancer cells. Interestingly, MDA-MB-231 cells are trying to pump out DOX-mwCNT-25 over the time course of 36 h, whereas the elimination of pure DOX began to decline after 6 h (Figure 5F). On the basis of the observed efflux of DOX-mwCNT-25, it was extrapolated that 100% efflux will occur after 60 h (Figure 5E). Although pure mwCNTs slightly down-regulated mRNA expression of *Mrp-1* during the initial 36 h in comparison to controls, no notable statistical difference was observed in protein level compared to control (Figure 5G). To confirm this, mwCNT were pretreated on MDA-MB-231 and showed normal efflux ability for post-treated DOX (Supporting Information Figure S9). As such, it is evident that mwCNTs do not intrinsically trigger the pumping behavior associated with cancer cell efflux, but only activate efflux when covalently conjugated with DOX.

Liver Toxicity, Inflammation, and Self-Clearance. Toxicity evaluation on liver is a critical factor in preclinic evaluation of newly designed DOX-mwCNT-25 because the liver accumulated the highest biodistribution of DOX-mwCNT as shown in Figure 2B,C. Although selective accumulation of CNTs in the liver is a commonly observed phenomenon, no comprehensive studies have further investigated CNT toxicity on liver to date.[24,25] As such, short- and long-term toxicity effects of mwCNT accumulation in the liver were scrutinized in this study. The mice were administered with three doses of 5 mg/kg of DOX-mwCNTs by intravenous (iv) injection and sacrificed for inspection of liver. As expected, increased dosage of DOX-mwCNT resulted in greater mwCNT accumulation in the liver and increased turbidity (opacity) (Figure 6A). However, glutamic oxaloacetic transaminase (GOT) and glutamic pyruvic transaminase (GPT) levels for all dosage groups remained within normal ranges (Figure 6B). Normal ranges were defined by the levels observed in the control group treated with PBS. Analysis of the inflammatory response, as determined by cytokine levels of tumor necrosis factor (TNF)-α, interleukin (IL)-2, IL-6 , and interferon (INF)-γ, demonstrated no significant variation from normal ranges (order of pg/mL) (Figure 6B). The distinct color difference of the liver between DOX-mwCNTs groups (*i.e.*, 0.5 and 5 mg/kg) was due to the difference in mwCNTs accumulation and did not result from liver toxicity. Furthermore, it is speculated that biocirculation will clear the liver turbidity over time, similar to the clearance of dispersed swCNTs from the lung.[50] Response to lower and higher levels of mwCNTs (*i.e.*, mwCNT-1 and mwCNT-2, corresponding to 2 and 20 mg/kg of mwCNT concentration, respectively) resembled results from 0.5 and 5 mg/kg of DOX-mwCNT-25. Specifically, a noticeable reduction in liver turbidity was observed after three months, suggesting that the accumulated CNTs had undergone clearance by biocirculation (Figure 6C). In H&E staining, a high amount of accumulated mwCNTs was observed between hepatocytes after one week (Figure 6D). After four weeks, mwCNT aggregation began undergoing the self-clearance process. By three months, a majority of mwCNTs were cleared and only trace amounts of mwCNTs remained. It is worthy to note that GOT, GPT and major cytokines (*i.e.*, TNF-α, IL-2, IL-6 and INF-γ) of mwCNT groups for 1, 4, and 12 weeks showed no notable difference compared to the control group (see Supporting Information Figure S16 for more detail). Thus, the obtained results demonstrated self-clearance for accumulated DOX-mwCNTs through blood-circulatory system as time advanced.

DISCUSSION AND CONCLUSION

Reducing drug amount for the treatment of various tumors can substantially increase life quality of patients during chemotherapy treatment. In this regard, authors focused on the development a low dose anticancer drug by nullifying cancer resistance without cotreatment with other drugs. Although biodistribution of used nanoparticles induced selective deposition in specific organs, this selective deposition of anticancer drug by intrinsic shape of materials can be oppositely harnessed for treatment of tumors at specific organs. In summary, the present study discussed several original findings. First, the designed covalently conjugated DOX-mwCNT showed high stability in the extracellular system. This is a critical factor in drug design, as the attached drug on nanomaterials should remain stable before and after reaching cancer cells, without prerelease in blood or drug storing solvent (neutral PBS). Second, it was observed that intaked DOX-mwCNTs were transported by endocytosis (possibly as clathrin or caveolae mediated endocytic pathway for nanosized

nanoparticles as discussed by previous studies[48]) and subsequently, delivered by early and late endosomes within cancer cells. The advantage to this mode of transportation is that it does not encounter direct drug pumping out from cytosol[51] and can increase drug retention time through endosome–lysosome delivery, as confirmed by high resolution images of late endosome and lysosome markers. Greater sizes of endosomes were observed after 10 h by means of small endosome fusion, and greater size of endosomes are assumed as early stage of endosomes since late endosome markers did not overlap (see Figure 5B). As expected, the mRNA and protein level of *Mrp-1* expression showed constant pumping to discharge intaked DOX-mwCNT over the initial 36 h, whereas *Mrp-1* functions began diminishing after 6 h for pure DOX samples. Lastly, burst drug release to cancer nucleus during late endosome and lysosome (or endolysosome) stages was identified for the first time. In this line, maximized release of DOX-mwCNT was observed in acidic lysozyme conditions that resemble the inner lumen of late endosomes and lysosomes, while developed drugs were highly stable under both neutral and acidic conditions (Figure 4J). Considering the most abundant lysozyme density was observed in the vicinity of cancer nuclei, it was speculated that drug release by cleavage of the covalent conjugation of nanodrugs began at the vicinity of nuclei with the abundant presence of hydrolase proteins, such as lysozymes. Through this proposed mechanism, the developed DOX-mwCNT can reduce the efficacious dosage of DOX anticancer drug by 10-fold *in vivo*. No remarkable liver toxicity was observed by three times injection of DOX-mwCNT and accumulated mwCNTs were underwent clearance over time.

The developed hybrid nanomaterials–drug system (DOX-mwCNT) is not only compatible with DOX, but also amenable to other types of anticancer drugs including most drugs having amine structures, such as epirubicin and daunorubicin. As such, the proposed design suggests a platform technology for achieving efficacy at low drug dosages through stable amide bonds. The primary outcome of this study is demonstration of a promising avenue for reducing side effects in patients and increasing patients' quality of life through the use of low dose anticancer nanodrug treatment.

MATERIALS AND METHODS

Carboxylation of mwCNTs. Purified mwCNTs (900-1351, SES) were preheated at 300 °C for 3 h to remove vapor and contaminants and oxidized to generate carboxyl groups. To generate carboxyl groups, 3:1 ratio of H_2SO_4/HNO_3 solution was sonicated with mwCNT in a water bath for 99 min and stirred with a magnetic bar for 36 h at 50 °C. Next, the solution was sonicated again for 15 min and filtered by mesh (100 μm), diluted with deionized (DI) water (1:200 v/v), and filtered (200 nm pore size PTFE, Millipore) with wash out several times to remove any residual solvent. mwCNTs were then dried in a vacuum oven at 60 °C overnight.

Materials Characterization. Carboxyl groups presented on the CNT surface were visualized with high resolution field-emission transmission electron microscopy (FE-TEM, JEM 2100F, Japan) operating at 200 kV. The measured diameter for the mwCNT was between 30 and 50 nm, as identified by TEM (data not shown). All mwCNT samples were diluted in ethanol and sonicated for 2 min before undergoing TEM procedures. Cryo-Transmission Electron Microscopy (Cryo-TEM, F20, Tecnai) was used to visualize covalently linked DOX on mwCNTs on a copper grid (plasma etched before dipping DOX-mwCNT solution). Next, prepared samples were instantly frozen in ethane and preserved in liquid nitrogen, using a plunge freezing technique in Vitrobot (FEI). Fourier transform infrared spectroscopy (FTIR, VERTEX 80v, Bruker Optics) was performed to analyze carboxyl formation on swCNTs. Samples were prepared by grinding the CNTs in an agate mortar with KBr and subjected to 70 MPa of applied pressure. The transparent flakes were analyzed within the mid-infrared wavelengths (400–4000 cm^{-1}). Quantitative analysis of the weight amount of functionalized groups (carboxyl) was performed by thermal gravimetric analysis (TGA: Q50, TA Instrument). Ten milligrams of mwCNTs was heat-treated at 60 °C for 3 h in vacuum before TGA to evaporate residual water molecules from the surfaces. TGA was performed with increasing temperature at a rate of 10 °C/min and under nitrogen flow at 100 mL/min. Particle size analysis (Zetasizer Nano, Malvern, U.K.) was performed to determine the particle size of DOX, mwCNT (Carboxylate), and DOX-mwCNT-25 at the density of 10 μg/mL. The UV–visible spectroscopy (X-ma 3000, Human Cooperation, South Korea) determined the loading amount of DOX on mwCNTs. DOX-mwCNT in PBS was diluted about 10–30 times to measure the absorbance peak. All standards curves from mwCNT and DOX were used to measure the loading amount. To measure the bonding strength between DOX and mwCNTs, luminescence spectrometer (Perkin-Elmer) was used. Quenching ratio was defined as the percent reduction from pure DOX fluorescence (set to 100%) and physically mixed (mixture by pipetting) DOX with mwCNT (set as 100%), respectively. To identify the amide bonds between DOX and mwCNT, Raman analysis (785 nm, LabRam Aramis, Horiba Jobin Yvon) was performed to examine any surface chemical changes by functionalization bonds.

Covalent Conjugation of DOX with mwCNTs. The carboxyl mwCNTs were dispersed in MES buffer (50 mM, pH 5.5) by tip sonication (Misonix 4000) with condition of 6 W, with frequency of 3 s-on/3 s-off for 5 min. Next, 400 mM NHS (*N*-hydroxysuccinimide, Sigma) solution in MES buffer (2-morpholinoethanesulfonic acid, 50 mM at pH 5.5) was added to the carboxylate mwCNT solution and stirred by vortex. This process served to increase the coupling efficiency by 10–20-fold in cross-linkage with EDC (1-ethyl-3-(dimethylaminopropyl)carbodiimide hydrochloride). The coupling pH condition in MES buffer was set to 6.1. EDC (300 mM in MES buffer solution, Sigma) was then added to the solution, and the mixture was stirred for 30 min. The mixture solution was then dispensed into filter tubes (AmiconYM-50, Millipore), centrifuged at 3000 rpm for 10 min, and rinsed with 50 mM MES buffer at least three times. EDC linked COOH-mwCNT solutions were then mixed with DOX (Sigma) at a weight ratio of 1:1 in MES buffer (the pH was set to 6.1). The mixture was agitated at 4 °C (refrigerator) at least 24 h. The DOX-mwCNT-conjugated suspensions in MES were centrifuged in AmiconYM-50 filter tubes at 3000 rpm for more than 3 times, to remove unconjugated drugs. Last, DOX-mwCNTs were dispersed in PBS. To measure the concentration of DOX and mwCNTs, UV–vis was used and adsorption analysis was performed at 490 nm to evaluate the DOX and mwCNT concentration. Covalently attached DOX weight percentage on mwCNT was determined by difference of absorbance signal intensities between DOX-mwCNT and weight density in solutions were

extrapolated by linear standard curves of DOX and oxidized mwCNTs. DOXIL (Doxoves, Liposomal Doxorubicin HCl) was purchased and diluted in PBS (pH = 7.2).

Drug Release Analysis. DOX-mwCNTs with an initial concentration of 1 μg/mL in PBS (pH 7.2) was added in acetate buffered saline (ABS, pH 5.0) and FBS 10% (pH 7.2). The percentage of DOX desorption was based on the total amount of initial DOX (set to 100%). Experimental samples (PBS, ABS, and FBS 10%) were suspended by gentle inversion and subsequently incubated at 37 °C. At each time point, the sample was centrifuged with 50 kDa ultrafilter (Millipore) with a 15 000 rpm for 15 min, and 500 mL of supernatant was taken at 1, 2, 5, 10, 24, 48, 72, 144, and 288 h. Individual solutions of DOX-MWCNT were prepared and kept at −20 °C. DOX fluorescence (emission at 590 nm; excitation at 470 nm) in the supernatant was measured with a microplate reader (TECAN, Switzerland).

Cell Assays. MCF-7 and MDA-MB-231 (5×10^3 cells/well, HTB-22, HTB-26, ATCC) were cultured in 96-well plates with DMEM supplemented with 10% of FBS in a humidified incubator at 37 °C with 5% of CO_2 level. After 24 h, the media was replaced with drug-fortified (*e.g.*, DOX and DOX-mwCNT) DMEM at 100 μL/well. An MTT assay was performed on cell cultures after 48 h. Briefly, cell media was replaced with MTT assay solution (1 mg/mL concentration; 100 μL/well volume) and allowed to incubate for 1 h at 37 °C. DMSO reagent (100 μL/well) was added in each well, and the absorbance was measured at 560 nm using a microplate reader (#680, Bio-Rad). For *in vivo* concentration test (or low concentration), distribution percentage was calculated from the biodistribution. If the weight of mice was 20 g, 0.5 and 5 mg/kg correspond to 10 and 100 μg of drug allocation, respectively, in tumor tissues (based on 2% allocation in tumor).

Actin and Morphology Analysis. Cells were cultured on poly-D-lysine-coated coverslips for 48 h and fixed with 4% paraformaldehyde in medium overnight at 4 °C. Permeabilization was done in PBS with 0.1% Triton X-100 for 15 min at room temperature. After a blocking period of 2 h with 1% of bovine serum albumin (BSA, AMRECO) in PBS, cells were incubated with F-actin (1:500, Invitrogen, Carlsbad, CA) antibody overnight at 4 °C in the absence of light. After a washing step, cells were mounted using ProLong Gold antifade reagent with DAPI (Invitrogen) stains. Cells were visualized using fluorescence microscopy (Olympus, Japan) with metamorph analysis (Olympus, Japan).

Analysis of DOX Influx and Efflux. MDA-MB-231 human breast cancer cells were cultivated in DMEM (11885-084, GIBCO) media supplemented with 10% heat-inactivated fetal bovine serum (16000-044, GIBCO), 100 U/mL penicillin and 100 μg/mL streptomycin (1% antibiotics) under standard cell culture conditions (5% CO_2 at 37 °C). For time-dependent DOX efflux assay, cells were seeded at a cell density of 5×10^3 cells/cm^2 on coverslips coated with poly-D-lysine (Sigma, St. Louis, MO). For influx analysis, MDA-MB-231 cells were pretreated with DOX-mwCNTs and DOX at concentrations of 12.5, 25, 50, 100, and 200 ng/mL for 2 h (influx) and cultured in unmodified media for 12 h (influx and efflux). For efflux analysis, cells were treated with 100 ng/mL of DOX after overnight incubation in normal media. After 2 h, cells on the DOX-fortified media were washed 3 times with 1× PBS and the solution was exchanged with regular media. After incubation for 0, 2, 6, 12, and 24 h in regular media, cells were fixed in 3.5% of PBS-neutral buffered paraformaldehyde (NBP) solution for 30 min at 4 °C and washed 3 times with 1× PBS. Samples were mounted onto slide glasses with an antifade reagent (ProLong, Invitrogen). Cells were imaged with fluorescence microscopy (BX51, Olympus) and analyzed with Meta Morph software (Olympus). DOX intensity was measured using ImageJ 1.46r software.

Immunocytochemistry Analysis of Lysozyme, Late Endosome, and Lysosome. Cells were cultured overnight on poly-D-lysine-coated coverslips and were treated with 100 ng/mL of pure DOX and DOX-mwCNT for 12 h. Cells were fixed with 4% paraformaldehyde in medium overnight at 4 °C. Permeabilization was performed by PBS with 0.1% Triton X-100 for 15 min at room temperature. After a blocking period of 2 h with 3% of bovine serum albumin (BSA, Amresco) in PBS, cells were incubated with lysozyme (1:200, ab2408, Abcam), mannose 6-phosphate receptor (late endosome marker, 1:1000, ab2733, Abcam), and LAMP1 (lysosome marker, 1:100, ab25630, Abcam) antibodies overnight at 4 °C in the absence of light. After they were washed thrice with 1× PBS, cells were incubated with Alexa Fluor488 Goat Anti-Rabbit IgG (H+L) and Alexa Fluor 680 Goat Anti-Mouse IgG (H+L) (1:200, A11008, A21057, Molecular Probes) for 1.5 h at room temperature. After the washing step, cells were mounted and visualized using fluorescence microscopy (Olympus, Japan) with metamorph analysis (Olympus, Japan).

Reverse Transcriptional-PCR. The mRNA expression of the human multidrug resistance-associated protein 1 (MRP-1) was evaluated to analyze efflux by cancer cells. RNA was isolated with Trizol reagent (Invitrogen, Carlsbad, CA). and 1 μg of RNA was reverse transcribed for synthesis of first cDNA strand. Synthesized cDNA was used as a template in PCR using PCR premix (Intron, South Korea) with pairs of primers for MRP-1 (forward, 5′-TCATCCTTGCTCTCTACCTC-3′; reverse, 5′-AGGTAGGCAGACTTCTTCAG-3′, 283 bp product) and GAPDH (forward, 5′-AGCTGAACGGGAAGCTCACT-3′; reverse, 5′-TGCTTAGCCAAATTCGTTG-3′, 300 bp product). PCR products were separated on 1.5% agarose gel and visualized by ethidium bromide staining.

Western Blot. Samples were rinsed twice with ice-cold PBS, and total cell lysates were gathered in 200 μL of lysis buffer (20 mM Tris-HCl, 120 mM NaCl, 50 mM HEPES, 1% Triton-X, 1 mM EDTA, 2 mM sodium orthovanadate, 1 mM DTT, 10% glycerol, 0.02 mM PMSF, 1 mg/mL leupeptin, and 1 mg/mL aprotinin). The lysates were spun in a microcentrifuge for 20 min at 4 °C, and the supernatant was collected. Proteins were electrophoresed using 8−12% SDS-PAGE, and then transferred to nitrocellulose membranes. The membranes were stained with reversible Ponceau S to ascertain equal loading of samples in the gel. MRP-1 was assayed using anti-MRP-1 antibody (sc-7774, Santa Cruz Biotech). Actin was determined using anti-actin antibodies (sc-8432, Santa Cruz Biotech). Immunodetection was performed using an enhanced chemiluminescence detection kit (34080, Thermo Scientific).

Biodistribution of DOX and DOX-mwCNT. All animal experiments were performed under the guidelines of the Animal Care Committee in Gyeongsang National University (Approval No. GLA-110920-M0038). Tumor models were established by subcutaneous inoculation with MDA-MB-231cells (*i.e.*, 5×10^6 cells per mouse) in the flank of female BALB/c *nu/nu* (athymic nude) mice (6−8 weeks). After 14 days of MDA-MB-231 xenograft, tumor-bearing mice were sacrificed for biodistribution experiments. First, 0.2 mL of DOX-mwCNT conjugates in PBS at a concentration of 2 mg/kg was injected into the tail vein. Treated mice were sacrificed at 30 min and at 6 h, and blood circulation was measured (from 15 μL of blood). For the DOX extraction, blood samples were dissolved in a lysis buffer-1 (defined by 1% SDS, 1% Triton X-100, 40 mM Tris-acetate, 10 mM EDTA, and 10 mM DTT), and DOX measurements were performed in accordance with previously reported protocols.[26] The blood samples in 1 mL of 0.75 M HCl in isopropyl alcohol (IPA) were incubated at −20 °C overnight. DOX fluorescence from the supernatant after centrifugation with 15 000 rpm for 20 min was measured using a fluorescence microplate reader. For DOX measurement, organs and tissues (0.1−0.2 g wet-weight) were homogenized in 0.5 mL of lysis buffer-2 (containing 0.25 M sucrose, 40 mM Tris-acetate, and 10 mM EDTA) using a homogenizer. To quantify DOX amount, 200 μL of tissue lysate was mixed with 100 μL of 10% Triton X-100. After strong vortex, 1 mL of extraction solution (0.75 M HCl in IPA) was added and the samples were incubated at −20 °C overnight. After centrifugation at 15 000 rpm for 20 min, fluorescence from the supernatant was measured.

Mouse Tumor Xenograft. MDA-MB-231 cells were inoculated subcutaneously in the flank of female BALB/c *nu/nu* (athymic nude) mice (5×10^6 cells per mouse) When the tumor reached a mean volume of 100 mm^3 (approximately 14 days after inoculation), the mice were randomly divided into seven groups ($n = 10$ per group) and injected with 200 μL of 0.5 mg/kg DOX, mwCNT, DOX-mwCNT in PBS, or pure PBS (negative control) in the tail vein. Subjects were weighed at 2, 9, and 16 days. Body weight and tumor sizes were measured twice a week for

21 days, and tumor volumes were calculated by the formula: V (volume) = X (length) × D (width)^2/2. After 21 days, mice were sacrificed and tumor weights were measured.

Histological Analysis. Tissues from the tumor and liver were dissected and fixed with 4% (NBP). The tissues were treated with paraffin, sectioned at a thickness of 1−5 μm, stained with H&E, and examined by optical microscopy (Olympus). Immunohistochemistry of tumor tissues was performed using the Ki-67 (Millipore, St. Charles, MO) antibody to identify proliferating cancer cells in tumor tissues. Deparaffinized tissue slides from tumors were placed in a solution of 3% of H_2O_2 for 10 min. After a washing step with 0.05 M Tris-HCl buffered saline (T buffer, pH 7.4), slides were incubated in diluted blocking serum for 30 min. Tumor tissues were then incubated at 4 °C overnight with Ki-67 (1:100, 5% goat serum in wet chamber). After a washing step, slides were incubated with a secondary biotinylated antibody (1:200). After they were washed thrice with T buffer, slides were incubated in avidin−biotin−peroxidase complex (ABC) solution (Vector Laboratories, Burlingame, CA) developed with 0.05% diaminobenzidine (DAB, Sigma) containing 0.01% H_2O_2. Tumor tissues were visualized using a BX51 light microscope (Olympus, Japan) and analyzed with the program (Olympus, Japan).

Clearance Analysis. BALB/c *nu/nu* (athymic nude) mice injected with 0.2 mL of DOX-mwCNT-25 conjugates at a dosage of 5 mg/kg three times were sacrificed after 1, 3, and 12 weeks, dissected, and fixed in 4% NBP. Blood samples from test groups were analyzed for various cytokines, GOT, and GPT levels under the supervision from Green Cross Corp. (http://www.greencross.com/eng/main.do, South Korea).

Statistical Analysis. The statistical differences between several sample types were analyzed with ANOVA followed by the Newman-Keuls' multiple comparison test. Asterisks (*, **, and ***) indicated the significance of p values less than 0.05, 0.01, and 0.001, respectively.

Conflict of Interest: The authors declare no competing financial interest.

Acknowledgment. Thanks for valuable comments from Dr. Hyun Shik Lee in Kyungpook National University and Dr. Sung Jean Park in Gachon University. This research was supported by grants from the medical research (MRC, 2012-0000304), Korea Food and Drug Administration (KFDA), and National Research Foundation (2010-0003359, 2012R1A1A2041157, PRC and 2012R1A2A1A01006546) from South Korea.

Supporting Information Available: Additional figures and results including materials properties of carboxylate mwCNTs; order of covalent linkage and associated quenching; Raman spectroscopy; viability and lysozyme densities of NIH3T3 and MCF7 cells; MDA-MB-231 cell viability; influx and efflux analysis; co-staining with DOX and late endosome on MDA-MB-231 cells; MRP-1 expression; diffusion of DOX from DOX-mwCNTs; *in vivo* antiproliferation on DOX and DOX-mwCNTs; levels of GOT, GPT and various cytokines. This material is available free of charge *via* the Internet at http://pubs.acs.org.

REFERENCES AND NOTES

1. Pennock, G. D.; Dalton, W. S.; Roeske, W. R.; Appleton, C. P.; Mosley, K.; Plezia, P.; Miller, T. P.; Salmon, S. E. Systemic Toxic Effects Associated with High-Dose Verapamil Infusion and Chemotherapy Administration. *J. Natl. Cancer Inst.* **1991**, *83*, 105–110.
2. Martin, M.; Lluch, A.; Segui, M. A.; Ruiz, A.; Ramos, M.; Adrover, E.; Rodriguez-Lescure, A.; Grosse, R.; Calvo, L.; Fernandez-Chacon, C.; *et al.* Toxicity and Health-Related Quality of Life in Breast Cancer Patients Receiving Adjuvant Docetaxel, Doxorubicin, Cyclophosphamide (TAC) or 5-Fluorouracil, Doxorubicin and Cyclophosphamide (FAC): Impact of Adding Primary Prophylactic Granulocyte-Colony Stimulating Factor to the TAC Regimen. *Ann. Oncol.* **2006**, *17*, 1205–1212.
3. Lindley, C.; McCune, J. S.; Thomason, T. E.; Lauder, D.; Sauls, A.; Adkins, S.; Sawyer, W. T. Perception of Chemotherapy Side Effects Cancer *versus* Noncancer Patients. *Cancer Pract.* **1999**, *7*, 59–65.
4. Vriesendorp, H. M.; Vriesendorp, R.; Vriesendorp, F. J. Prediction of Normal Tissue Damage Induced by Cancer Chemotherapy. *Cancer Chemother. Pharmacol.* **1987**, *19*, 273–276.
5. Swain, S. M.; Whaley, F. S.; Ewer, M. S. Congestive Heart Failure in Patients Treated with Doxorubicin: A Retrospective Analysis of Three Trials. *Cancer* **2003**, *97*, 2869–2879.
6. Zitvogel, L.; Apetoh, L.; Ghiringhelli, F.; Kroemer, G. Immunological Aspects of Cancer Chemotherapy. *Nat. Rev. Immunol.* **2008**, *8*, 59–73.
7. Longley, D. B.; Johnston, P. G. Molecular Mechanisms of Drug Resistance. *J. Pathol.* **2005**, *205*, 275–292.
8. Szakacs, G.; Paterson, J. K.; Ludwig, J. A.; Booth-Genthe, C.; Gottesman, M. M. Targeting Multidrug Resistance in Cancer. *Nat. Rev. Drug Discovery* **2006**, *5*, 219–234.
9. Sridhar, R.; Dwivedi, C.; Anderson, J.; Baker, P. B.; Sharma, H. M.; Desai, P.; Engineer, F. N. Effects of Verapamil on the Acute Toxicity of Doxorubicin *in Vivo*. *J. Natl. Cancer Inst.* **1992**, *84*, 1653–1660.
10. Yahanda, A. M.; Alder, K. M.; Fisher, G. A.; Brophy, N. A.; Halsey, J.; Hardy, R. I.; Gosland, M. P.; Lum, B. L.; Sikic, B. I. Phase I Trial of Etoposide with Cyclosporine as a Modulator of Multidrug Resistance. *J. Clin. Oncol.* **1992**, *10*, 1624–1634.
11. Allen, T. M.; Cullis, P. R. Drug Delivery Systems: Entering the Mainstream. *Science* **2004**, *303*, 1818–1822.
12. Peer, D.; Karp, J. M.; Hong, S.; Farokhzad, O. C.; Margalit, R.; Langer, R. Nanocarriers as an Emerging Platform for Cancer Therapy. *Nat. Nanotechnol.* **2007**, *2*, 751–760.
13. Wang, F.; Wang, Y. C.; Dou, S.; Xiong, M. H.; Sun, T. M.; Wang, J. Doxorubicin-Tethered Responsive Gold Nanoparticles Facilitate Intracellular Drug Delivery for Overcoming Multidrug Resistance in Cancer Cells. *ACS Nano* **2011**, *5*, 3679–3692.
14. Gao, Y.; Chen, Y.; Ji, X.; He, X.; Yin, Q.; Zhang, Z.; Shi, J.; Li, Y. Controlled Intracellular Release of Doxorubicin in Multidrug-Resistant Cancer Cells by Tuning the Shell-Pore Sizes of Mesoporous Silica Nanoparticles. *ACS Nano* **2011**, *5*, 9788–9798.
15. Milane, L.; Duan, Z.; Amiji, M. Development of EGFR-Targeted Polymer Blend Nanocarriers for Combination Paclitaxel/Lonidamine Delivery To Treat Multi-Drug Resistance in Human Breast and Ovarian Tumor Cells. *Mol. Pharmaceutics* **2011**, *8*, 185–203.
16. Chow, E. K.; Zhang, X. Q.; Chen, M.; Lam, R.; Robinson, E.; Huang, H.; Schaffer, D.; Osawa, E.; Goga, A.; Ho, D. Nanodiamond Therapeutic Delivery Agents Mediate Enhanced Chemoresistant Tumor Treatment. *Sci. Transl. Med.* **2011**, *3*, 73ra21.
17. Li, R.; Wu, R.; Zhao, L.; Wu, M.; Yang, L.; Zou, H. P-Glycoprotein Antibody Functionalized Carbon Nanotube Overcomes the Multidrug Resistance of Human Leukemia Cells. *ACS Nano* **2010**, *4*, 1399–1408.
18. Arora, H. C.; Jensen, M. P.; Yuan, Y.; Wu, A.; Vogt, S.; Paunesku, T.; Woloschak, G. E. Nanocarriers Enhance Doxorubicin Uptake in Drug-Resistant Ovarian Cancer Cells. *Cancer Res.* **2012**, *72*, 769–778.
19. Meng, H.; Liong, M.; Xia, T.; Li, Z.; Ji, Z.; Zink, J. I.; Nel, A. E. Engineered Design of Mesoporous Silica Nanoparticles to Deliver Doxorubicin and P-Glycoprotein siRNA to Overcome Drug Resistance in a Cancer Cell Line. *ACS Nano* **2010**, *4*, 4539–4550.
20. Abbasi, M.; Aliabadi, H. M.; Moase, E. H.; Lavasanifar, A.; Kaur, K.; Lai, R.; Doillon, C.; Uludag, H. siRNA-Mediated Down-Regulation of P-Glycoprotein in a Xenograft Tumor Model in NOD-SCID Mice. *Pharm. Res.* **2011**, *28*, 2516–2529.
21. Xiong, X. B.; Lavasanifar, A. Traceable Multifunctional Micellar Nanocarriers for Cancer-Targeted Co-Delivery of MDR-1 siRNA and Doxorubicin. *ACS Nano* **2011**, *5*, 5202–5213.
22. Aigner, A. Gene Silencing through RNA Interference (RNAi) *in Vivo*: Strategies Based on the Direct Application of siRNAs. *J. Biotechnol.* **2006**, *124*, 12–25.

23. Lu, P. Y.; Xie, F.; Woodle, M. C. *In Vivo* Application of RNA Interference: From Functional Genomics to Therapeutics. *Adv. Genet.* **2005**, *54*, 117–142.
24. Liu, Z.; Cai, W.; He, L.; Nakayama, N.; Chen, K.; Sun, X.; Chen, X.; Dai, H. *In Vivo* Biodistribution and Highly Efficient Tumour Targeting of Carbon Nanotubes in Mice. *Nat. Nanotechnol.* **2007**, *2*, 47–52.
25. Liu, Z.; Chen, K.; Davis, C.; Sherlock, S.; Cao, Q.; Chen, X.; Dai, H. Drug Delivery with Carbon Nanotubes for *in Vivo* Cancer Treatment. *Cancer Res.* **2008**, *68*, 6652–6660.
26. Liu, Z.; Fan, A. C.; Rakhra, K.; Sherlock, S.; Goodwin, A.; Chen, X.; Yang, Q.; Felsher, D. W.; Dai, H. Supramolecular Stacking of Doxorubicin on Carbon Nanotubes for *in Vivo* Cancer Therapy. *Angew. Chem., Int. Ed.* **2009**, *48*, 7668–7672.
27. Liu, Z.; Sun, X.; Nakayama-Ratchford, N.; Dai, H. Supramolecular Chemistry on Water-Soluble Carbon Nanotubes for Drug Loading and Delivery. *ACS Nano* **2007**, *1*, 50–56.
28. Tong, L.; Liu, Y.; Dolash, B. D.; Jung, Y.; Slipchenko, M. N.; Bergstrom, D. E.; Cheng, J. X. Label-Free Imaging of Semiconducting and Metallic Carbon Nanotubes in Cells and Mice Using Transient Absorption Microscopy. *Nat. Nanotechnol.* **2012**, *7*, 56–61.
29. Kam, N.; Liu, Z.; Dai, H. Carbon Nanotubes as Intracellular Transporters for Proteins and DNA: An Investigation of the Uptake Mechanism and Pathway. *Angew. Chem., Int. Ed.* **2006**, *45*, 577–581.
30. Kostarelos, K.; Lacerda, L.; Pastorin, G.; Wu, W.; Wieckowski, S.; Luangsivilay, J.; Godefroy, S.; Pantarotto, D.; Briand, J. P.; Muller, S.; Prato, M.; Bianco, A. Cellular Uptake of Functionalized Carbon Nanotubes Is Independent of Functional Group and Cell Type. *Nat. Nanotechnol.* **2007**, *2*, 108–113.
31. Cheng, J.; Fernando, K. A.; Veca, L. M.; Sun, Y. P.; Lamond, A. I.; Lam, Y. W.; Cheng, S. H. Reversible Accumulation of PEGylated Single-Walled Carbon Nanotubes in the Mammalian Nucleus. *ACS Nano* **2008**, *2*, 2085–2094.
32. Schipper, M. L.; Nakayama-Ratchford, N.; Davis, C. R.; Kam, N. W.; Chu, P.; Liu, Z.; Sun, X.; Dai, H.; Gambhir, S. S. A Pilot Toxicology Study of Single-Walled Carbon Nanotubes in a Small Sample of Mice. *Nat. Nanotechnol.* **2008**, *3*, 216–221.
33. De la Zerda, A.; Zavaleta, C.; Keren, S.; Vaithilingam, S.; Bodapati, S.; Liu, Z.; Levi, J.; Smith, B. R.; Ma, T. J.; Oralkan, O.; *et al.* Carbon Nanotubes as Photoacoustic Molecular Imaging Agents in Living Mice. *Nat. Nanotechnol.* **2008**, *3*, 557–562.
34. Liu, Z.; Tabakman, S. M.; Chen, Z.; Dai, H. Preparation of Carbon Nanotube Bioconjugates for Biomedical Applications. *Nat. Protoc.* **2009**, *4*, 1372–1382.
35. Prabaharan, M.; Grailer, J. J.; Pilla, S.; Steeber, D. A.; Gong, S. Gold Nanoparticles with a Monolayer of Doxorubicin-Conjugated Amphiphilic Block Copolymer for Tumor-Targeted Drug Delivery. *Biomaterials* **2009**, *30*, 6065–6075.
36. Zhang, X.; Meng, L.; Lu, Q.; Fei, Z.; Dyson, P. J. Targeted Delivery and Controlled Release of Doxorubicin to Cancer Cells Using Modified Single Wall Carbon Nanotubes. *Biomaterials* **2009**, *30*, 6041–6047.
37. Min, K. H.; Kim, J. H.; Bae, S. M.; Shin, H.; Kim, M. S.; Park, S.; Lee, H.; Park, R. W.; Kim, I. S.; Kim, K.; *et al.* Tumoral Acidic pH-Responsive MPEG-Poly(beta-amino ester) Polymeric Micelles for Cancer Targeting Therapy. *J. Controlled Release* **2010**, *144*, 259–266.
38. Huang, W. C.; Chiang, W. H.; Huang, Y. F.; Lin, S. C.; Shih, Z. F.; Chern, C. S.; Chiang, C. S.; Chiu, H. C. Nano-Scaled pH-Responsive Polymeric Vesicles for Intracellular Release of Doxorubicin. *J. Drug Targeting* **2011**, *19*, 944–953.
39. Wu, W.; Li, R.; Bian, X.; Zhu, Z.; Ding, D.; Li, X.; Jia, Z.; Jiang, X.; Hu, Y. Covalently Combining Carbon Nanotubes with Anticancer Agent: Preparation and Antitumor Activity. *ACS Nano* **2009**, *3*, 2740–2750.
40. Fabbro, C.; Ali-Boucetta, H.; Da Ros, T.; Kostarelos, K.; Bianco, A.; Prato, M. Targeting Carbon Nanotubes Against Cancer. *Chem. Commun. (Cambridge, U.K.)* **2012**, *48*, 3911–3926.
41. Gu, Y. J.; Cheng, J.; Jin, J.; Cheng, S. H.; Wong, W. T. Development and Evaluation of pH-Responsive Single-Walled Carbon Nanotube-Doxorubicin Complexes in Cancer Cells. *Int. J. Nanomed.* **2011**, *6*, 2889–2898.
42. Yang, R.; Jin, J.; Chen, Y.; Shao, N.; Kang, H.; Xiao, Z.; Tang, Z.; Wu, Y.; Zhu, Z.; Tan, W. Carbon Nanotube-Quenched Fluorescent Oligonucleotides: Probes That Fluoresce upon Hybridization. *J. Am. Chem. Soc.* **2008**, *130*, 8351–8358.
43. Chiu, C. F.; Dementev, N.; Borguet, E. Fluorescence Quenching of Dyes Covalently Attached to Single-Walled Carbon Nanotubes. *J. Phys. Chem. A* **2011**, *115*, 9579–84.
44. Ballesteros, B.; Torre Gde, L.; Ehli, C.; Rahman, G. M.; Agullo-Rueda, F.; Guldi, D. M.; Torres, T. Single-Wall Carbon Nanotubes Bearing Covalently Linked Phthalocyanines-Photoinduced Electron Transfer. *J. Am. Chem. Soc.* **2007**, *129*, 5061–5068.
45. Chidawanyika, W.; Nyokong, T. Characterization of Amine-Functionalized Single-Walled Carbon Nanotube-Low Symmetry Phthalocyanine Conjugates. *Carbon* **2010**, *48*, 2831–2838.
46. Ali-Boucetta, H.; Al-Jamal, K. T.; McCarthy, D.; Prato, M.; Bianco, A.; Kostarelos, K. Multiwalled Carbon Nanotube-Doxorubicin Supramolecular Complexes for Cancer Therapeutics. *Chem. Commun. (Cambridge, U.K.)* **2008**, 459–461.
47. Baskaran, D.; Mays, J. W.; Zhang, X. P.; Bratcher, M. S. Carbon Nanotubes with Covalently Linked Porphyrin Antennae: Photoinduced Electron Transfer. *J. Am. Chem. Soc.* **2005**, *127*, 6916–6917.
48. Conner, S. D.; Schmid, S. L. Regulated Portals of Entry into the Cell. *Nature* **2003**, *422*, 37–44.
49. Worm, J.; Kirkin, A. F.; Dzhandzhugazyan, K. N.; Guldberg, P. Methylation-Dependent Silencing of the Reduced Folate Carrier Gene in Inherently Methotrexate-Resistant Human Breast Cancer Cells. *J. Biol. Chem.* **2001**, *276*, 39990–40000.
50. Mutlu, G. M.; Budinger, G. R.; Green, A. A.; Urich, D.; Soberanes, S.; Chiarella, S. E.; Alheid, G. F.; McCrimmon, D. R.; Szleifer, I.; Hersam, M. C. Biocompatible Nanoscale Dispersion of Single-Walled Carbon Nanotubes Minimizes *in Vivo* Pulmonary Toxicity. *Nano Lett.* **2010**, *10*, 1664–1670.
51. Cho, K.; Wang, X.; Nie, S.; Chen, Z. G.; Shin, D. M. Therapeutic Nanoparticles for Drug Delivery in Cancer. *Clin. Cancer Res.* **2008**, *14*, 1310–1316.